Electronic Supplementary Material (ESI) for Physical Chemistry Chemical Physics.

Supporting Information

Emergence of selectivity and specificity in a coarse-grained model of the nuclear pore complex with sequence-agnostic FG-Nups

Manoj Kumar Patel[1], Buddhapriya Chakrabarti[2] and Ajay Singh Panwar[1]*

[1]Department of Metallurgical Engineering and Materials Science, Indian Institute of Technology Bombay, Powai, Mumbai 400076, India

[2]Department of Physics, Sheffield University, UK

*Corresponding author: panwar@iitb.ac.in

Table of Contents **Page**

S1. Langevin dynamics simulations

All CG atoms in the simulation were assumed to execute Brownian motion in an implicit solvent. Their dynamics was described by the Langevin equation, S1 [1,2] ,

$$m_i \frac{d^2 r_i}{dt^2} = -\zeta v_i - \nabla_i U(r_{ij}) + F_i^r(t) + F_i^{ext} \quad \text{S1}$$

where, m_i, r_i, ζ, and v_i represented mass, position, damping coefficient and velocity of any particle i, respectively. The only exceptions were the CG atoms that made up the wall of the cylindrical pore, which were assumed to be immobile during the simulation. Random forces, F_i^r, acting on CG atoms were described by the fluctuation-dissipation theorem described in S2,

$$\langle F_i^r(t) F_j^r(t') \rangle = 6\zeta k_B T \delta(t - t') \delta_{ij}, \quad \text{S2}$$

A constant, downward external force, $F_i^{ext} = F$, was applied to the tracer particle to nudge the tracer toward the NPC. This models the effect of Ran-GTP/GDP gradient in the biological scenario which confers directionality to cargo motion [3–8]. Although, the application of a constant force appears to be an over-simplified representation of a more complex process, it is meant to mimic the essential features of directional nucleocytoplasmic transport in our simple CG polymer-based model.

The net interaction potential, $U(r_{ij})$ was described as a sum of excluded volume interactions, U_{LJ}, and bond potentials, U_{bond} (for the copolymer chains) as shown in equation S3,

$$U(r_{ij}) = U_{LJ} + U_{bond}, \quad \text{S3}$$

The excluded volume interactions between any two CG beads were described by the Lennard-Jones interactions given by equation S4,

$$U_{Lj}(r_{ij}) = \begin{cases} 4\epsilon_{LJ}\left[\left(\frac{\sigma}{r_{ij}}\right)^{12}\right] - \left[\left(\frac{\sigma}{r_{ij}}\right)^{6}\right], & r_{ij} \leq 2.5\sigma \\ 0, & r_{ij} > 2.5\sigma \end{cases} \quad \text{S4}$$

where, ϵ_{LJ} and σ are the Lennard-Jones interaction parameter and van der Waals diameter, respectively. Bond potentials, U_{bond}, for freely-jointed copolymer chains were described by the FENE (finitely-extensible non-linear elastic) potential [9,10] as mentioned in equation S5,

$$U_{bond} = -\frac{1}{2}kR_{max}^2 \ln[1 - (r_b/R_{max})^2] \quad \text{S5}$$

where, maximum allowable distance between beads $R_{max} = 1.5l_0$, r_b is separation distance between any adjacent beads, l_0 is the bond length along the polymer chain and k is spring constant. The velocity-Verlet algorithm [2] was employed to solve equation 1 numerically with a timestep Δt of 0.001τ. Since, the Langevin equation was solved in the over-damped regime, the corresponding scale for time was described by $\tau = \zeta l_0^2/k_BT$s, where the Stokes drag coefficient is $\zeta = 6\pi\eta\sigma$. Correspondingly, the thermal energy, k_BT, was the scale for energy and k_BT/l_0 was the appropriate scale for force in the simulations.

S2. Langevin dynamics simulation scales

S2.1 Non-dimensionalisation of scales

The dimensionless simulation scales correspond to actual dimensional values in the following manner;

i. The scale for length, l_0, corresponds to approximately the size of two adjacent residues along a polypeptide chain, which is approximately 1 nm. Hence,

$$l_0 = 1 \equiv 1 \text{ nm}$$

ii. All simulations are relevant at the physiological temperature of 310 K. Therefore,

$$T = 1 \equiv 310 \text{ K}$$

iii. Thermal energy is used as the relevant scale for energy. Hence,

$$\epsilon = 1 \equiv k_B T$$

iv. Accordingly, force is defined as,

$$F = 1 \equiv \frac{\epsilon}{l_0} \equiv \frac{k_B T}{l_0} \equiv 4 \text{ pN}$$

v. A characteristic time-scale corresponding to a diffusion time is defined as,

$$\tau = 1 \equiv \frac{6\pi\eta a}{K_B T} l_0^2 = 22 \text{ ns}$$

which assumes a cellular viscosity of $\eta = 5$ cP [11,12]. However, this value was rounded off to $\tau = 20$ ns, which was chosen as the characteristic time-scale in the simulations.

S2.2 Rationalisation of choice of scales

1. Length scales:

   a. Nup length: In a yeast NPC, four rings (32 copies) of Nsp1 (≈ 600 residues) are present. In the current study, FG-Nups are modelled on Nsp1. In our coarse-graining scheme, every polymer united atom (bead) represents two adjacent amino acids. As a result, the FG-Nup length in the current study was $N = 300$. Whereas, the diameter of a polymer bead was 0.75 nm, the polymer (Nup) bond length was 1 nm. The bond length of 1 nm approximately corresponded to the size of two adjacent residues.

   b. Pore (NPC) dimensions: Whereas, the diameter of a typical NPC lies in the range 30 – 50 nm, the height (*or the axial extent across the nuclear membrane*) is reported to vary between 40 – 90 nm. In the current study, we considered a cylindrical pore for the NPC to represent the transmembrane part of the NPC. Hence, we used a diameter and height of 50 nm and 45 nm, respectively. Both numbers are in the range of reported dimensions of NPCs across various organisms [4,13,14].

   c. Tracer Diameter: Cargoes less than 5-6 nm or (40kDa) can passively diffuse through the pore, whereas cargoes larger than 5-6 nm require karyopherins to assist them in passage[6]. A typical karyopherin, such as importin-beta, is approximately 10 nm in size along the longest dimension. This implies that a cargo of a karyopherin-bound globular protein will be larger than this size. Hence, the choice of $d_t = 12$ nm for the tracer particle in the current study.

2 Energy scales:

a. In the current study, thermal energy, k_BT, was used as a fundamental scale for energy. This is significant since the FG-Nups have been shown to form a thermal, entropic brush *in situ* in experiments[15].

b. In addition, hydrophobic interactions between FG-FG segments and FG-receptor segments, are important because these interactions determine network formation and tracer transport through the pore. These were represented by Lennard-Jones (LJ) potentials and their values were consistent with LJ parameter values used in similar coarse-grained simulations by Baygi and coworkers[11]. In that study too, FG-receptor interactions were stronger in comparison to FG-FG interactions. According to the selective phase model, Kap can locally break down network crosslinks during cargo translocation because Kap-FG affinity is higher than FG-FG affinity[16]. The same hypothesis was also adopted in another simulation study by Ghavami and coworkers[17,18] to assess the FG-Nup dynamics inside the pore. The implication of the choice of the LJ parameters for various hydrophobic interactions is explained in more detail in Point number 3 (*on scales for force*).

3. Scales for force:

a. In the current study, a constant, downward external force, $F_i^{ext} = F_t$, was applied to the tracer particle to nudge the tracer toward the NPC. The magnitude of this force was $F_t = 2$ pN, which is approximately half of the thermal force in the system. This modelled the effect of Ran-GTP/GDP gradient in the biological scenario which confers directionality to cargo motion[3,7,8,19,20]. In a previous simulation study, Baygi and coworkers also used a small nudging force in their cargo translocation simulations through the pore, which acted as a guiding force to help the tracer find

the pore entry[20]. In their studies, the nudging force was on the order of the thermal noise and was varied between 0.25 – 4.5 pN.

b. In an experimental study, Otsuka and co-workers measured the FG-cargo binding/ rupture forces through single molecule force measurements[21]. Statistically, two different populations of rupture force were detected in their study, corresponding to a smaller (29$\pm$6.2 pN) and a larger (49$\pm$4.8 pN) force, respectively. The value of $F_t = 2$ pN is much smaller in comparison to the 30 – 50 pN rupture force measured between FG-Nups and receptors (importin-β). Further, they estimated 4 binding pockets for importin-β, which translates to a rupture force of 7 – 12 pN per binding pocket.

For the simulation parameters used in the current study, a calculation of the FG-receptor hydrophobic attractive force for $\epsilon_{26} = 1.5 - 2.0$ yielded a value of $F_{26} = 14 - 19$ pN for every FG bead-receptor bead contact. Although, this force was nearly two times that estimated by Otsuka *et al.*, it is remarkable that our coarse-grained description provided a close estimate of the rupture force. It should also be noted that the isotropic, spherical shape used for the tracer in the current study is an oversimplification of the three-dimensional shape of the karyopherin-cargo complex. A complex shape may result in variable accessibility of FG-Nups to FG-binding domains on karyopherins and accordingly affect the rupture forces.

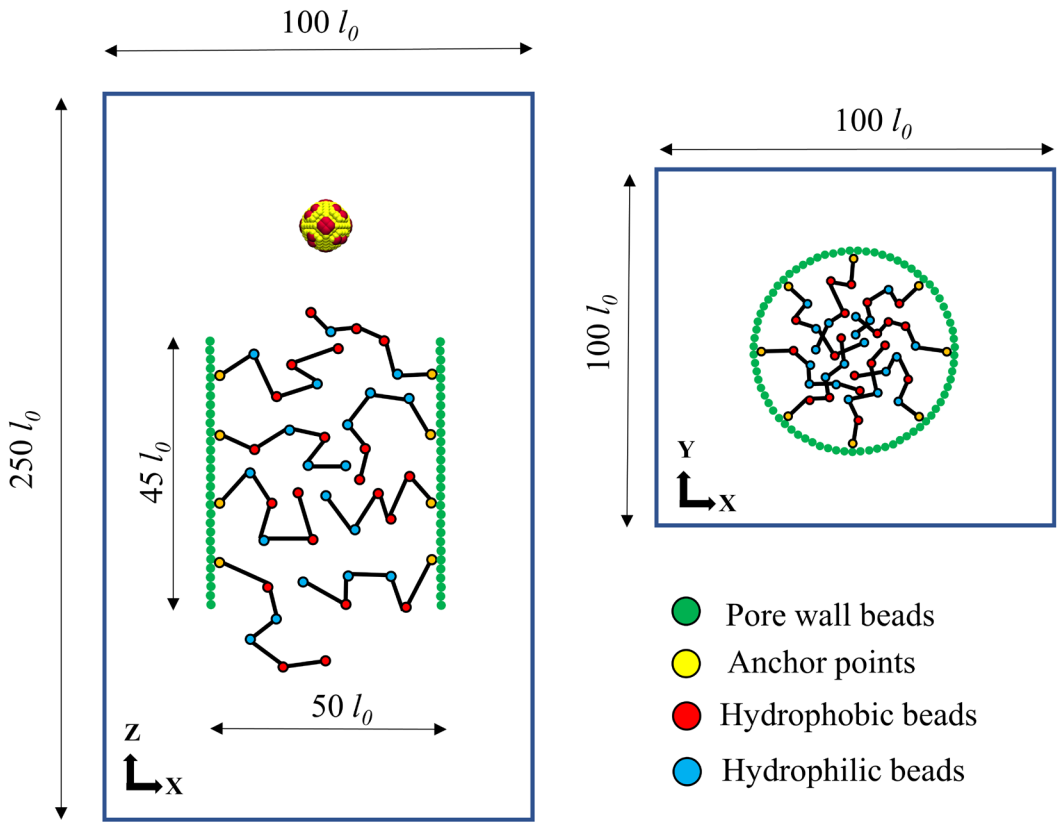

Figure S1. Schematic of simulation setup showing the simulation box dimensions and the coarse-grained description of both NPC and tracer.

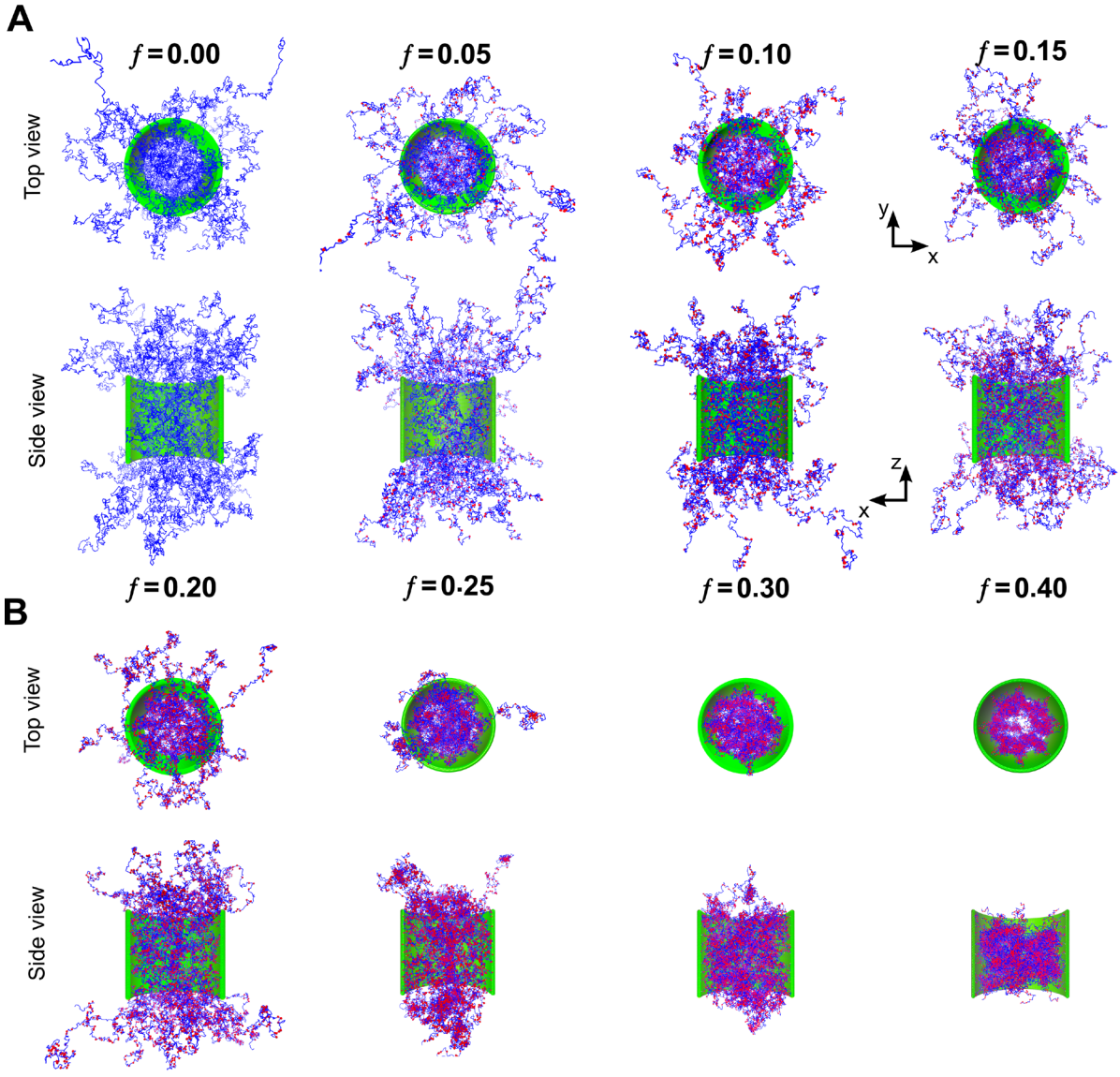

Figure S2. Simulation snapshots showing top and side views of equilibrium brush structures for the model NPC corresponding to (A) $f = 0, 0.05, 0.10, 0.15$, and (B) $f = 0.20, 0.25, 0.30, 0.40$.

S3. Stillinger algorithm for identifying clusters

FG-beads (type 2 beads) in the polymer brush formed dynamic crosslinks due to hydrophobic interactions. Collectively, these crosslinks gave rise to the formation of clusters inside the NPC. The Stillinger algorithm was used in the current work to identify and quantify the formation of clusters inside the cylindrical NPC pore [22,23].

Consider a system of N particles that interact with each other through a short-range pair potential, $V(r)$. An effective interaction distance, b, can be defined around each sphere within which pair interaction are significant enough to result in clustering of particles. Overlaps between neighboring spheres can then be obtained by drawing a sphere of radius $b/2$ around every particle. As shown in Figure S3, overlapping spherical regions define a cluster, C, constituted of all overlapping particles. If particle i belongs to a cluster, C, and $r_{ij} < b$, then j also belongs to C.

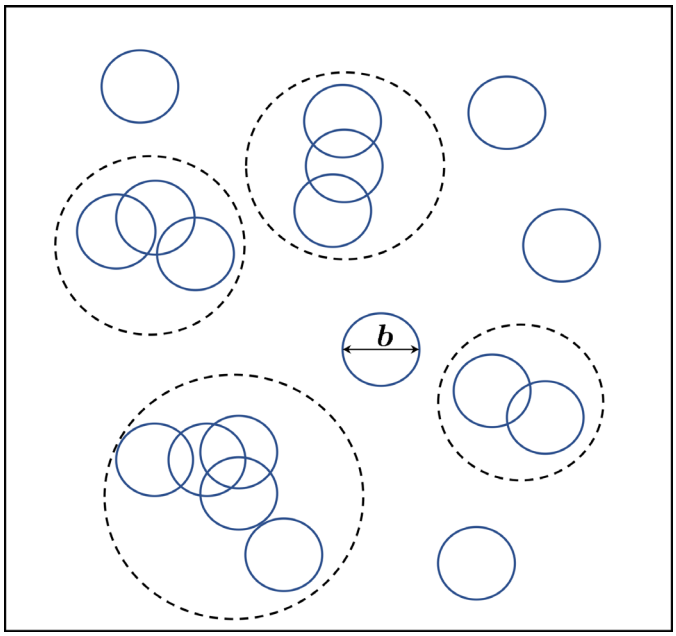

Figure S3. Cluster identification algorithm. Overlapped particles of radius b/2 forming clusters. 18 particles shown in configuration shows 1 cluster consisting of 2 particles, 2 clusters consisting of 3 particles and 1 cluster of 5 particles.

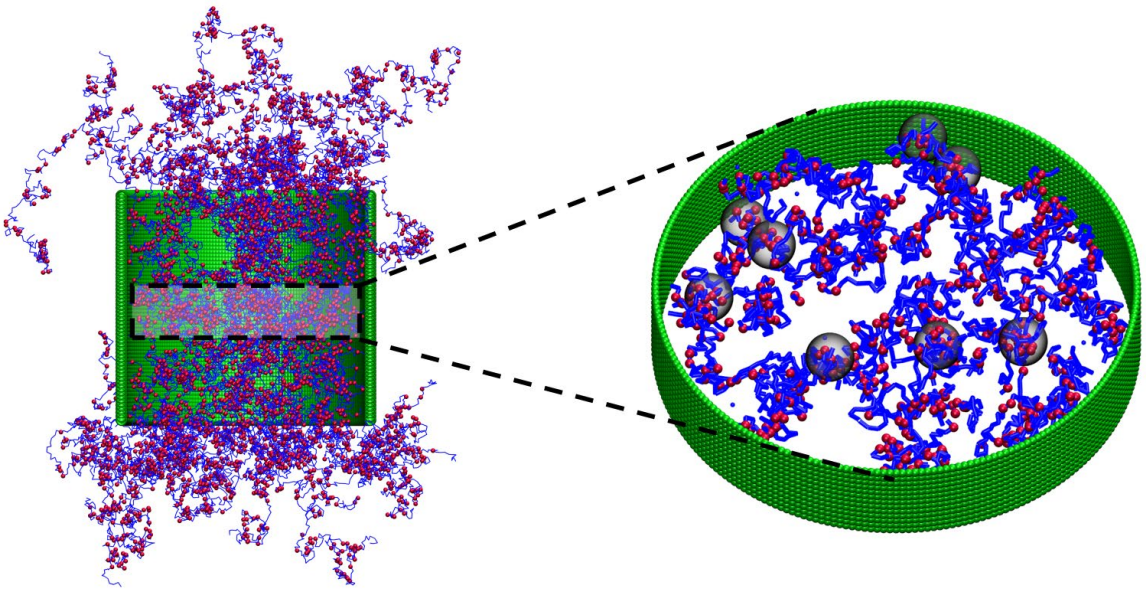

Figure S4. Snapshot of cluster formation inside the pore for $f = 0.2$. A part of the brush from only the middle section of the pore (left) is taken to highlight the formation of hydrophobic clusters in the region. Clusters are represented as transparent spheres containing crosslinked hydrophobic beads (right).

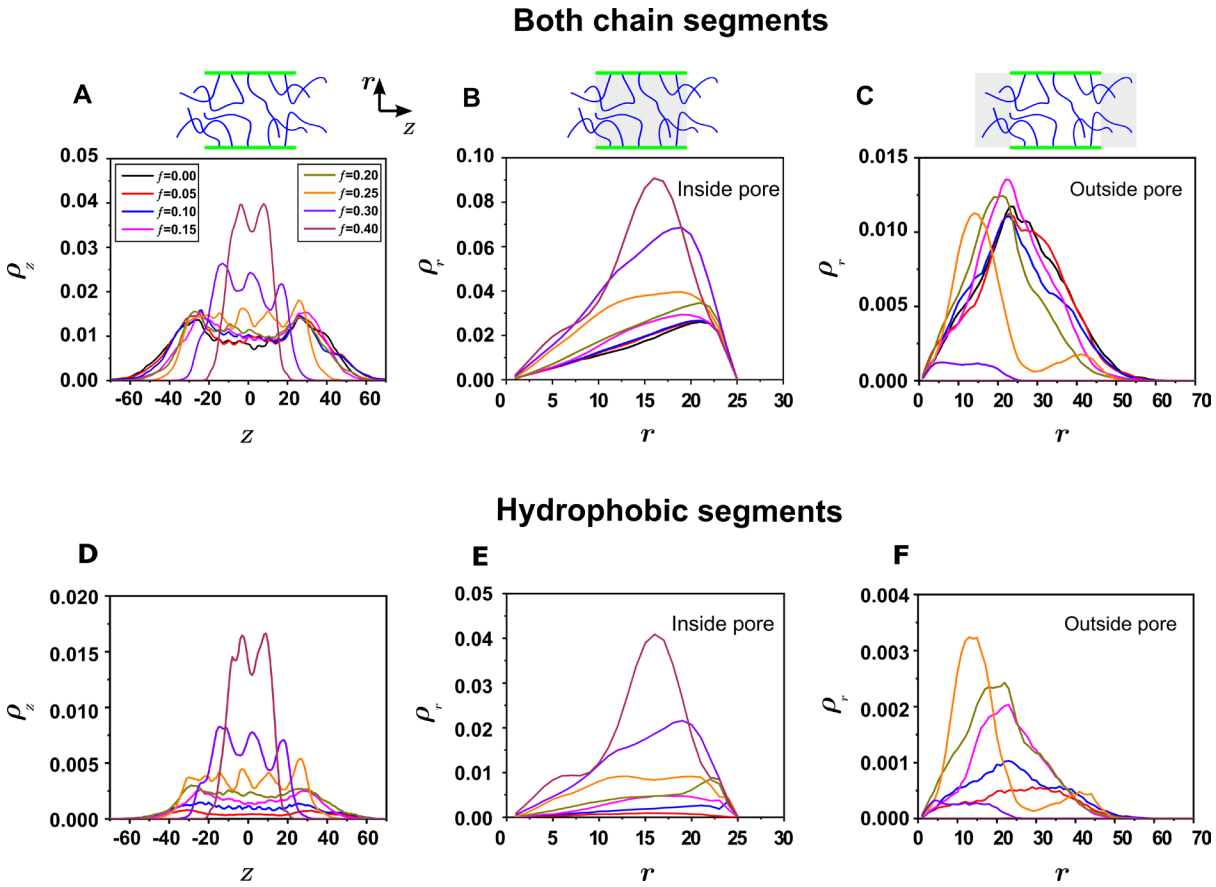

Figure S5. Plots showing equilibrated density distributions of brush segments calculated by considering, (A – C) both hydrophobic and hydrophilic segments, and (D – F) only hydrophobic segments. Density distributions were plotted along the (A, D) axial direction of the NPC, (B, E) radial direction of the NPC (inside the cylindrical region), and (C, F) radial direction of the NPC (outside the cylindrical region).

S4. Tracer trajectories for an inert tracer ($d_t = 6$ nm)

Nearly all trajectories simulated for inert tracers, $d_t = 6$ nm at F_t= 0.8 pN, were rejected by the NPC for all values of *f* (Figure S5 of the Supporting Information). The scale of thermal force in the simulation **is**, $k_BT/l_0 \approx 4$ pN. Hence, F_t= 0.8 pN was much weaker compared to the Brownian forces on tracers which prevented tracers from entering the NPC. In addition, the brush also offered a large entropic barrier to tracer entry at low *f* because of its significant expanse outside the pore. In contrast, all tracer trajectories of 6 nm inert particle translocated successfully at F_t= 4 pN for every hydrophobic fraction (Figure S6 of the Supporting Information). At low *f*, the tracer was small enough to pass through the open structure of the NPC. For $f \geq 0.3$, the tracer size was small enough to pass through the gaps in the tightly bound network structure. Typical translocation times of ≈ 0.5 ms were observed for F_t= 4 pN.

At an intermediate force of F_t= 2 pN, some differentiation in tracer response to the FG hydrophobic fraction was observed (Figure S7 of the Supporting Information). A simple back-of-the envelope calculation based on experimental measurements of concentration gradients shows that a value of F_t= 2 pN is appropriate in the biophysical [3]. Most of the 12nm tracer trajectories for $f \geq 0.25$ were either rejected or trapped by the NPC indicating a signature of pore selectivity with respect to the FG hydrophobic fraction, *f*. However, the motion of a 6 nm tracer corresponded to the case of passive translocation through the NPC not requiring transport receptors. In contrast, the larger 12 nm tracer corresponded to the case of facilitated transport across the NE aided by transport receptors (NTR/Kaps). This is also supported by reports in the literature [3–5].

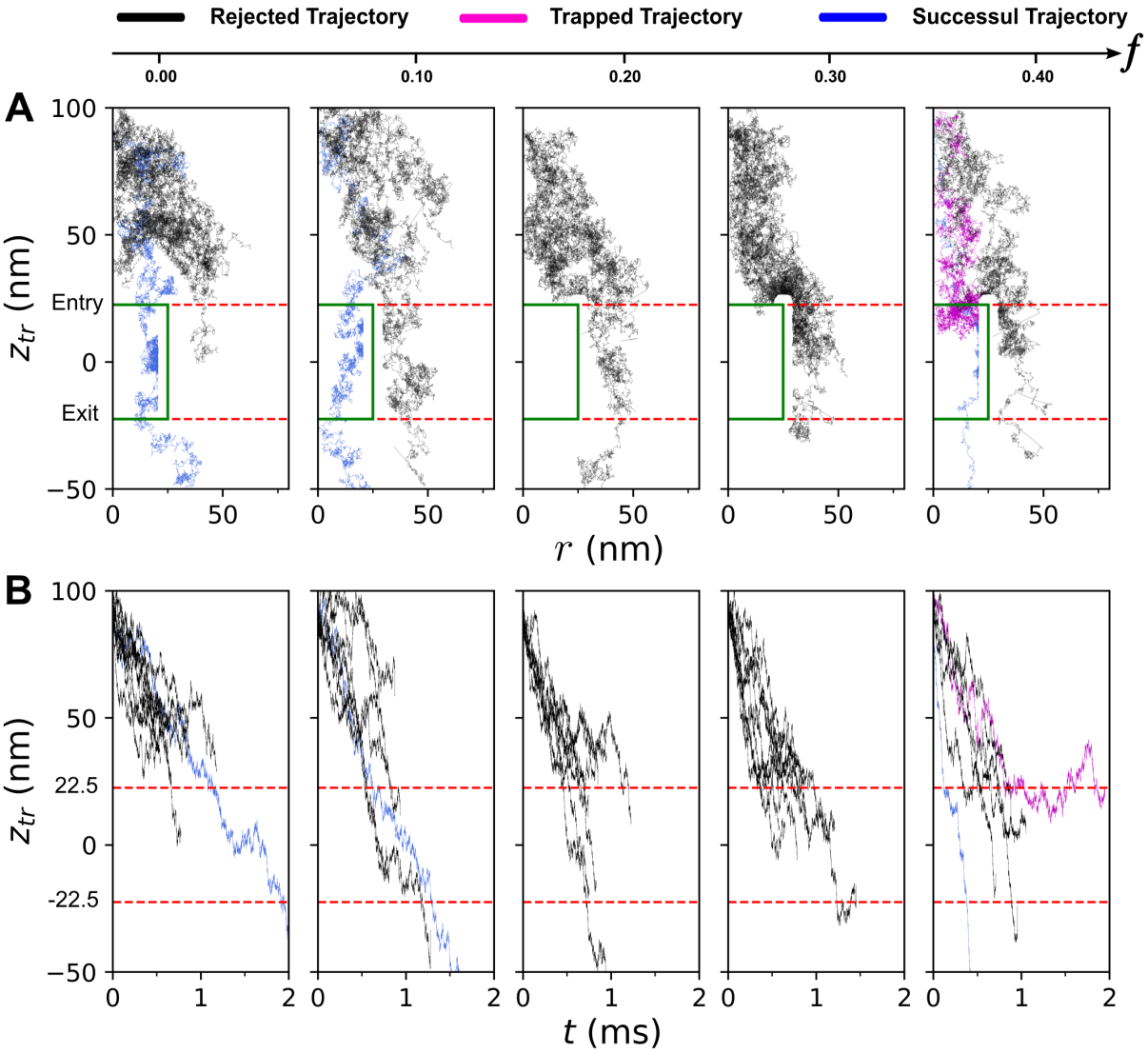

Figure S6. Inert tracer trajectories from ten independent simulations shown for different values of f corresponding to d_t= 6 nm, F_t = 0.8 pN. The simulated trajectories were classified into three types, *successful* (blue), *trapped* (pink) and *rejected* (black). Successful trajectories corresponded to tracers "successfully" entering the NPC and exiting from the other side. (A) Tracer paths during the simulations represented as z_{tr} *vs* r plots, where z_{tr} is the z-coordinate of the tracer, and r is tracer radial coordinate. (B) Plots showing the variation of z_{tr} with time, t.

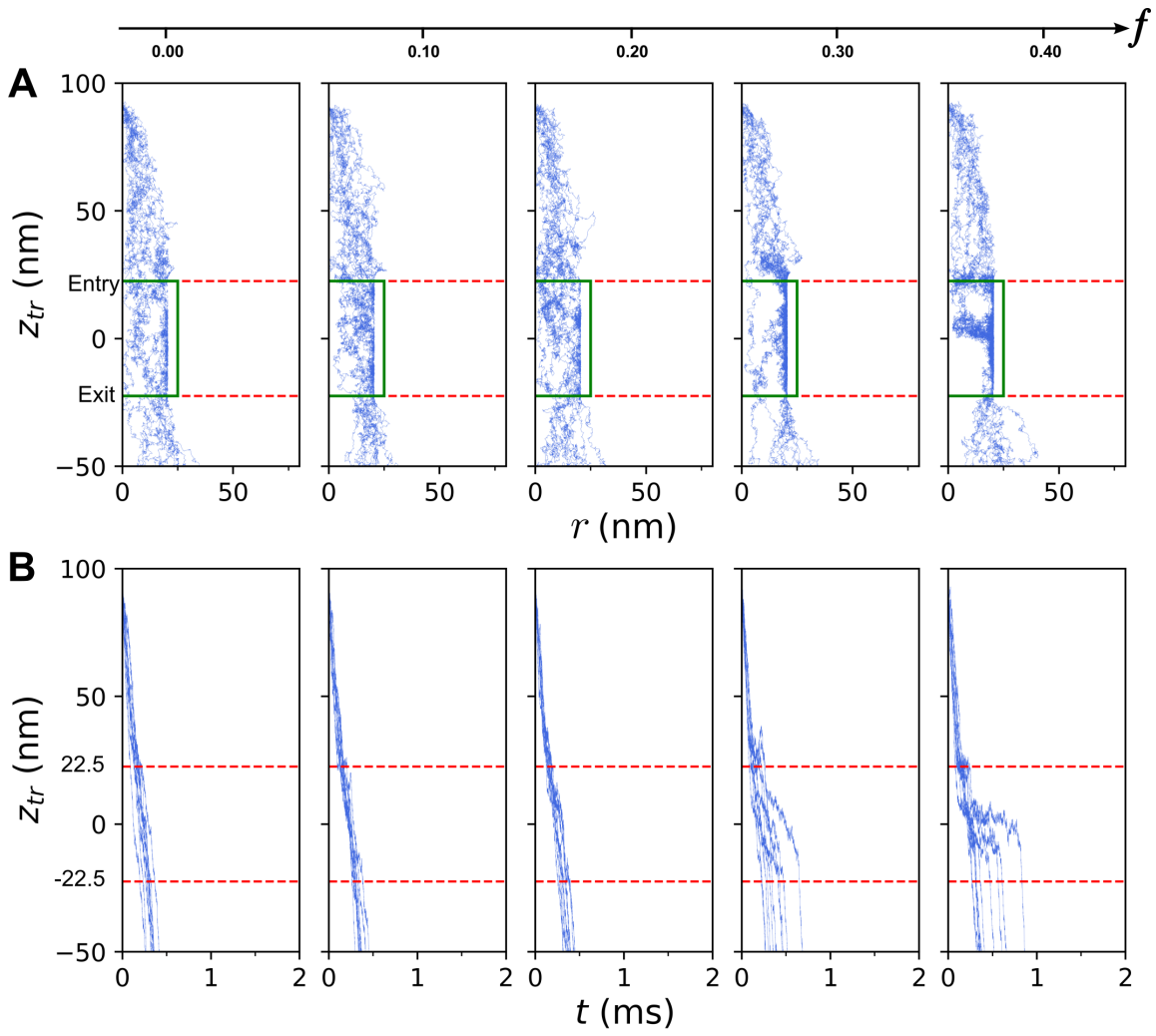

Figure S7. Inert tracer trajectories from ten independent simulations shown for different values of f corresponding to d_t= 6 nm, F_t = 4.0 pN. (A) Tracer paths during the simulations represented as z_{tr} *vs* r plots, where z_{tr} is the z-coordinate of the tracer, and r is tracer radial coordinate. (B) Plots showing the variation of z_{tr} with time, t.

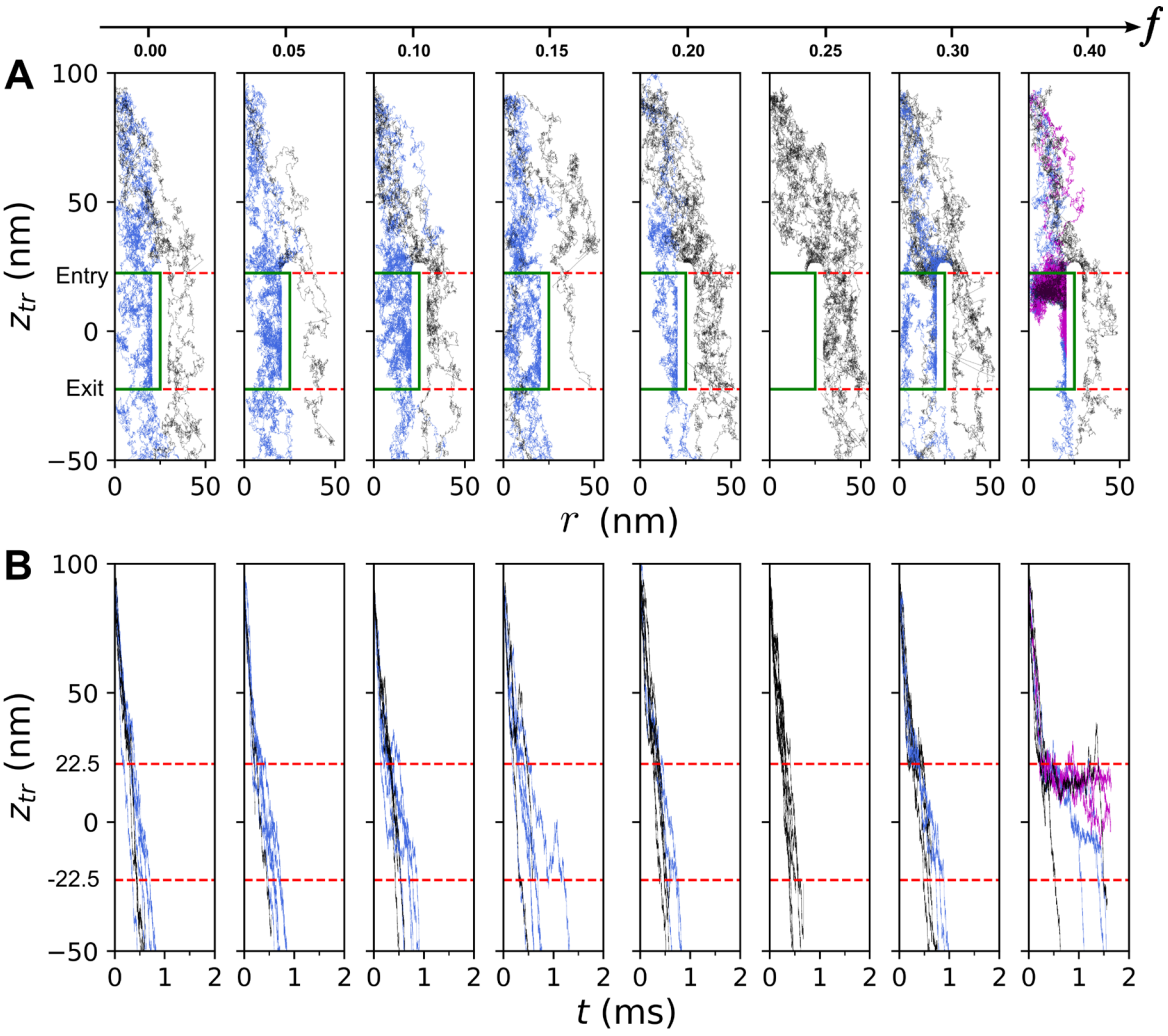

Figure S8. Inert tracer trajectories from ten independent simulations shown for different values of f corresponding to d_t= 6 nm, F_t = 2.0 pN. (A) Tracer paths during the simulations represented as z_{tr} *vs* r plots, where z_{tr} is the z-coordinate of the tracer, and r is tracer radial coordinate. (B) Plots showing the variation of z_{tr} with time, t.

S5. Tracer trajectories for inert and patchy tracers ($d_t = 12$ nm)

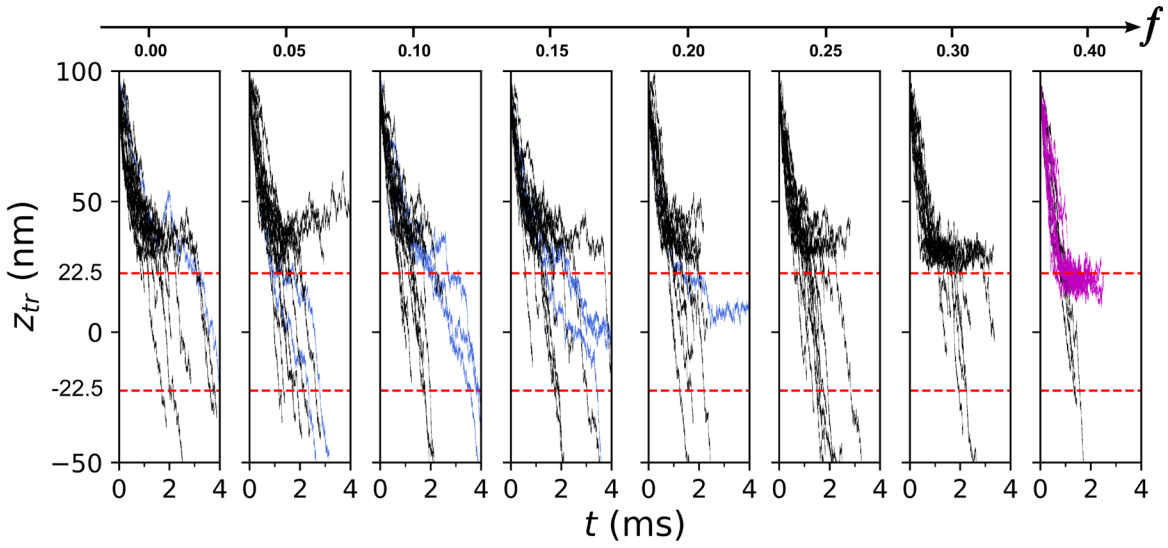

Figure S9. Inert tracer trajectories from twenty independent simulations shown for different values of f corresponding to d_t= 12 nm, F_t = 2.0 pN. Plots show the variation of z-coordinate of the tracer, z_{tr}, with time, t.

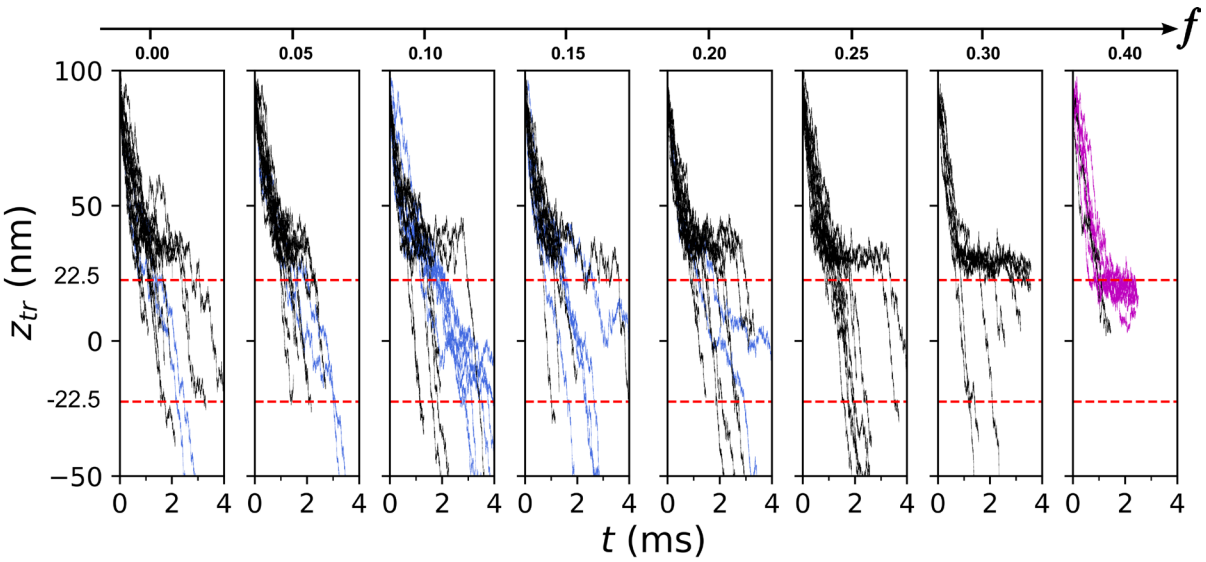

Figure S10. Patchy tracer trajectories from twenty independent simulations shown for different values of f corresponding to d_t= 12 nm, ϵ_{26} = 1.5, F_t = 2.0 pN. Plots show the variation of z-coordinate of the tracer, z_{tr}, with time, t.

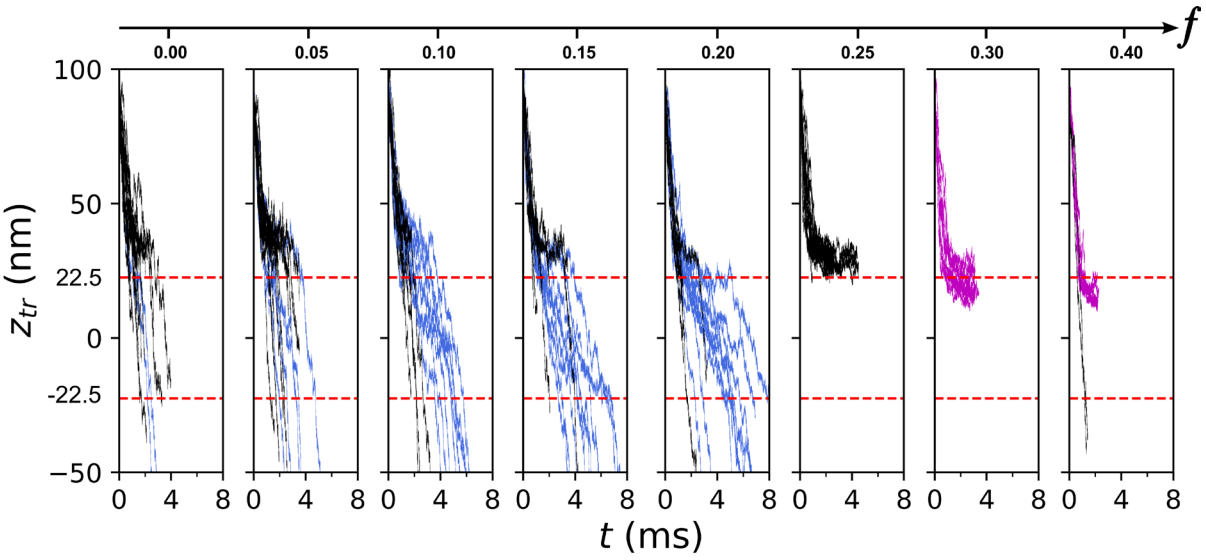

Figure S11. Patchy tracer trajectories from twenty independent simulations shown for different values of f corresponding to d_t= 12 nm, $\epsilon_{26} = 2.0$, $F_t = 2.0$ pN. Plots show the variation of z-coordinate of the tracer, z_{tr}, with time, t.

S6. Mesh size calculation

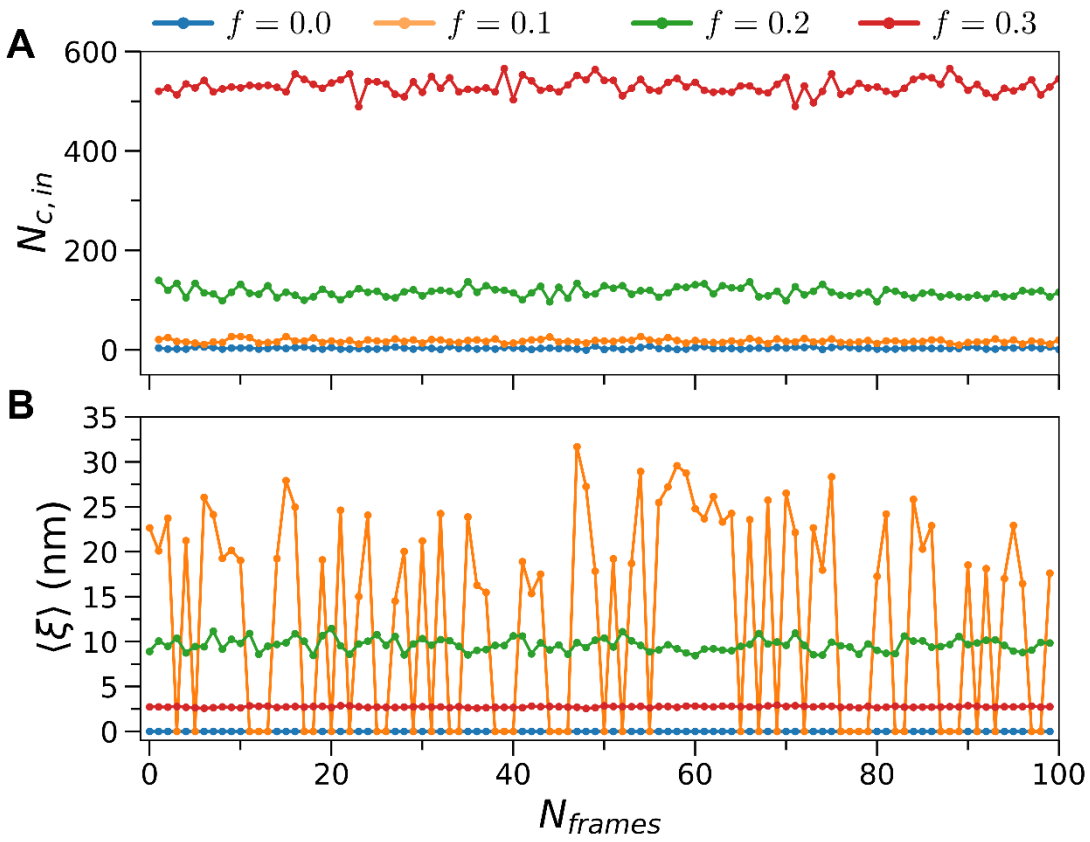

Figure S12. Mesh analysis of each frame for last 100 frames of equilibrated brush. (A) FG-FG crosslinks give rise to cluster formation throughout the pore. Plot showing number of clusters inside the pore, $N_{c,in}$ as a function of frames. (B) Plot of average mesh size calculated for every frame as a function of number of frames.

S7. Comparison of NPCs with $N = 200$ and $N = 300$

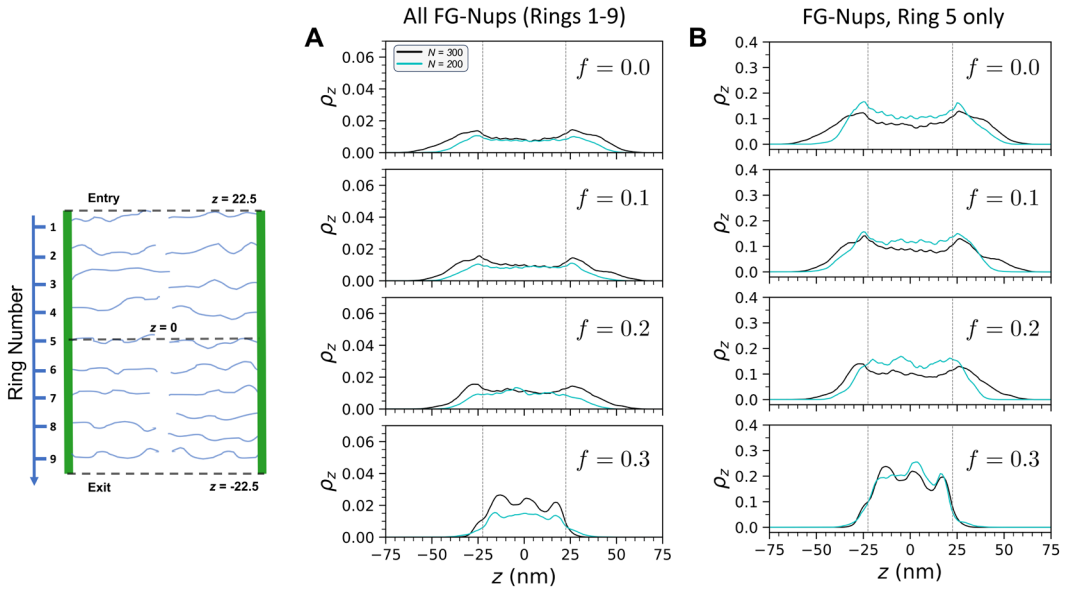

Figure S13. Plots comparing the equilibrated axial density distributions of brush segments for NPCs with $N = 200$ and $N = 300$, respectively, for different FG-hydrophobic fraction, $f = 0, 0.1, 0.2, 0.3$. (A) Axial density distributions of segments from FG-Nups from all 9 rings, (B) axial density distributions of segments belonging to only the middle ring (ring 5) located at the mid-plane of the pore at $z = 0$.

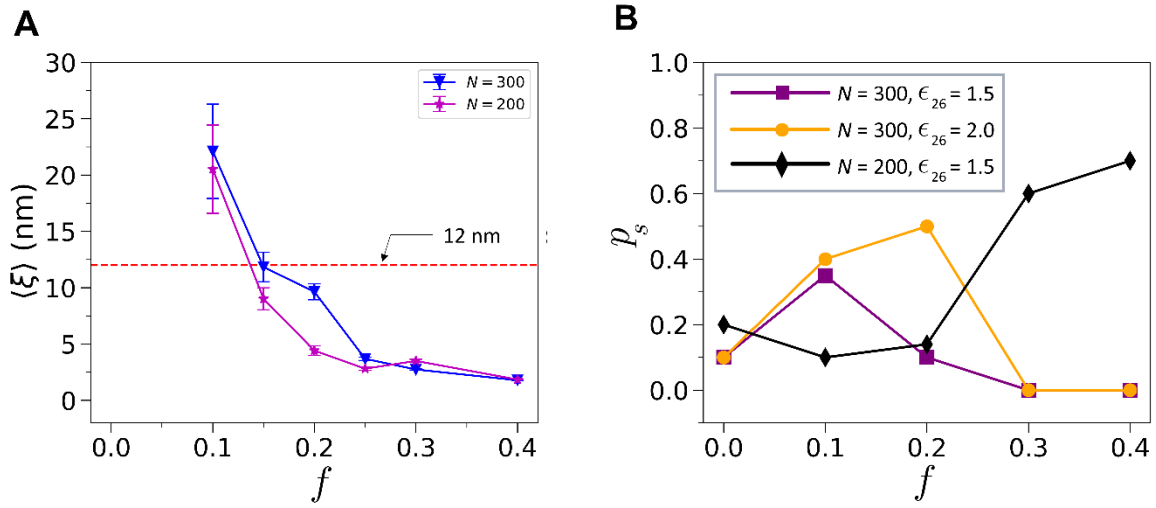

Figure S14. (A) Average mesh size inside the pore for chain lengths of $N = 300$ and $N = 200$ at different FG-hydrophobic fraction, f. (B) Probability of success through pores of chain length of $N = 300$ and $N = 200$ with varying tracer-brush interaction strength, ϵ_{26}. Probability of successful translocation, p_s, plotted as a function of f for patchy tracers translocating through NPCs with of $N = 300$ and $N = 200$, respectively. Both sets of simulations were carried out with $d_t = 12$ nm and $F_t = 2$ pN.

S8. Effect of mesh size on p_s

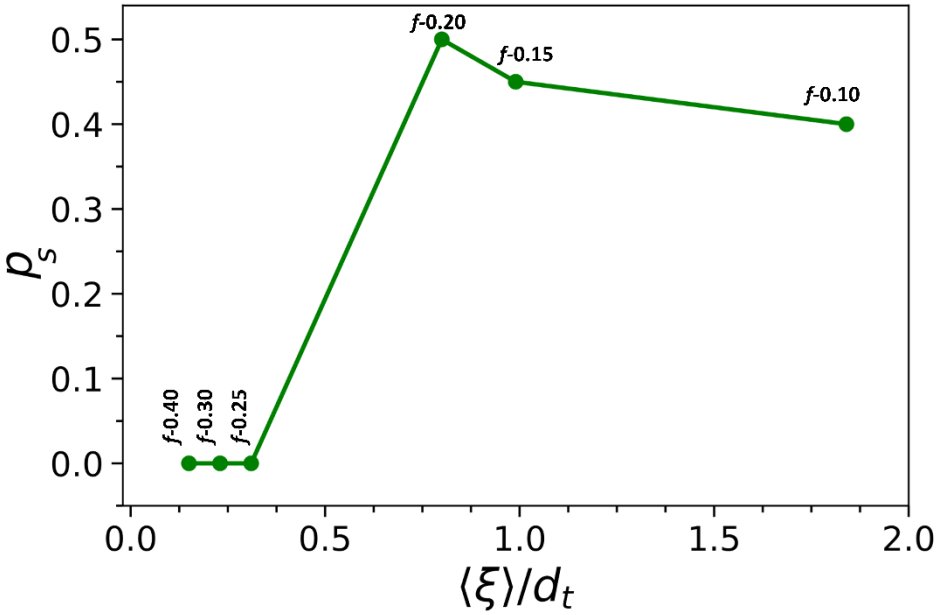

Figure S15. Probability of successful translocations, p_s, plotted as a function of reduced mesh size, $\langle\xi\rangle/d_t$.

REFERENCES

1 S. E. Feller, Y. Zhang, R. W. Pastor and B. R. Brooks, Constant pressure molecular dynamics simulation: The Langevin piston method, *J Chem Phys*, 1995, **103**, 4613–4621.

2 D. Frenkel, B. Smit, J. Tobochnik, S. R. McKay and W. Christian, Understanding Molecular Simulation, *Computers in Physics*, 1997, **11**, 351.

3 I. A. N. G. Macara, Transport into and out of the Nucleus, *Microbiology and Molecular Biology Reviews*, 2001, **65**, 570–594.

4 D. H. Lin and A. Hoelz, The Structure of the Nuclear Pore Complex (An Update), *Annu Rev Biochem*, 2019, **88**, 725–783.

5 I. V. Aramburu and E. A. Lemke, Floppy but not sloppy: Interaction mechanism of FG-nucleoporins and nuclear transport receptors, *Semin Cell Dev Biol*, 2017, **68**, 34–41.

6 R. Peters, Translocation through the nuclear pore: Kaps pave the way, *BioEssays*, 2009, **31**, 466–477.

7 D. Osmanović, A. Fassati, I. J. Ford and B. W. Hoogenboom, Physical modelling of the nuclear pore complex, *Soft Matter*, 2013, **9**, 10442–10451.

8 B. Ding and M. Sepehrimanesh, Nucleocytoplasmic transport: Regulatory mechanisms and the implications in neurodegeneration, *Int J Mol Sci*, 2021, **22**, 4165.

9 S. Plimpton, Fast parallel algorithms for short-range molecular dynamics, *J Comput Phys*, 1995, **117**, 1–19.

10 H. M. Aktulga, J. C. Fogarty, S. A. Pandit and A. Y. Grama, Parallel reactive molecular dynamics: Numerical methods and algorithmic techniques, *Parallel Comput*, 2012, **38**, 245–259.

11 R. Moussavi-Baygi, Y. Jamali, R. Karimi and M. R. K. K. Mofrad, Brownian dynamics simulation of nucleocytoplasmic transport: A coarse-grained model for the functional state of the nuclear pore complex, *PLoS Comput Biol*, 2011, **7**, e1002049.

12 D. Görlich, M. J. Seewald and K. Ribbeck, Characterization of Ran-driven cargo transport and the RanGTPase system by kinetic measurements and computer simulation, *EMBO J*, 2003, **22**, 1088–1100.

13 T. Zheng and A. Zilman, Self-regulation of the nuclear pore complex enables clogging-free crowded transport, *Proceedings of the National Academy of Sciences*, , DOI:10.1073/pnas.2212874120.

14 A. Goryaynov, J. Ma and W. Yang, Single-molecule studies of nucleocytoplasmic transport: from one dimension to three dimensions, *Integr. Biol.*, 2012, **4**, 10–21.

15 R. Y. H. Lim and J. Deng, Interaction forces and reversible collapse of a polymer brush-gated nanopore, *ACS Nano*, 2009, **3**, 2911–2918.

16 T. A. Isgro and K. Schulten, Cse1p-Binding Dynamics Reveal a Binding Pattern for FG-Repeat Nucleoporins on Transport Receptors, *Structure*, 2007, **15**, 977–991.

17 A. Ghavami, E. Van Der Giessen and P. R. Onck, Energetics of transport through the nuclear pore complex, *PLoS One*, 2016, **11**, 1–13.

18 A. Ghavami, L. M. Veenhoff, E. Van Der Giessen and P. R. Onck, Probing the disordered domain of the nuclear pore complex through coarse-grained molecular dynamics simulations, *Biophys J*, 2014, **107**, 1393–1402.

19 P. Kalab and R. Heald, The RanGTP gradient–a GPS for the mitotic spindle, *J Cell Sci*, 2008, **121**, 1577–1586.

20 R. Moussavi-Baygi and M. R. K. Mofrad, Rapid Brownian Motion Primes Ultrafast Reconstruction of Intrinsically Disordered Phe-Gly Repeats Inside the Nuclear Pore Complex, *Sci Rep*, 2016, **6**, 1–12.

21 S. Otsuka, S. Iwasaka, Y. Yoneda, K. Takeyasu and S. H. Yoshimura, Individual binding pockets of importin-β for FG-nucleoporins have different binding properties and different sensitivities to RanGTP, *Proceedings of the National Academy of Sciences*, 2008, **105**, 16101–16106.

22 S. D. Stoddard, Identifying Clusters in Computer Experiments on Systems of Particles, *J Comput Phys*, 1978, **27**, 291–293.

23 F. H. Stillinger Jr, F. H. Stillinger and F. H. Stillinger Jr, Rigorous basis of the Frenkel-Band theory of association equilibrium, *J Chem Phys*, 1963, **38**, 1486–1494.